AZIMUTHAL SHEAR WAVE ANISOTROPY ANALYSIS, GUIDED IN TIME DOMAIN

Marek Kozak, Mirka Kozak, Jefferson Williams, Supersonic Geophysical LLC

ABSTRACT

Ideally, waveform data excited by an acoustic dipole source should only generate Flexural waves. Unfortunately, other acoustic modes are also often created; including Stoneley or Compressional waves. Whether these undesired modes appear or not depends on tool position, well deviation, and borehole conditions. Classic shear wave anisotropy analysis can deliver erroneous values due to the presence of mixed acoustic modes within the processing window in time domain. Therefore, we propose to augment shear wave anisotropy analysis with waveform guiding in time domain. Flexural wave arrival time is tracked at each receiver station independently. This travel time searching procedure is repeated twice: first utilizing dipole XX (on axis) data, and then dipole YY (also on axis) data. During each of the passes, the faster arrival is selected, thus yielding the vector of depth domain curves that define zero phase arrival time at each receiver level independently. Under isotropic conditions with collocated transmitters, dipole XX and dipole YY zero phase arrival times will be the same. However, when the formation is anisotropic, these arrival times will differ according to the strength of the anisotropy field. Angular energy distributions can be calculated using the time domain tracking curves described above. These distributions are computed at each receiver station separately, yielding on axis E_{xx} and off axis E_{xy} angular energy fields. Since energy distribution computations are guided and performed within a relatively narrow time window, the possibility that non-flexural mode wave forms (e.g. Stoneley mode) contaminate the outcome is significantly reduced. We illustrate how to identify a mixed acoustic mode condition, and how to control the quality of maximum stress direction computations. We also show how to qualify cross dipole data using the instantaneous frequency/slowness analysis method. Various field examples are also presented.

INTRODUCTION

Cross-dipole logging tools are commonly used to measure formation anisotropic properties in a borehole environment. Shear wave anisotropy analysis is based on four-component waveform data, generated by two orthogonal dipole sources X and Y, and an array of orthogonal receivers. Since the sources and receivers are mounted orthogonally, the cross-dipole tool will excite two in-line (XX and YY), and two cross-line (XY and YX) sets of waveforms. In an isotropic formation at the low frequency limit, flexural wave propagation velocity will approach that of formation shear. In the case of an anisotropic formation, the flexural wave will split into slow and fast modes that travel with different velocities. Since polarizations of slow and fast flexural waves are aligned with these of formation shear waves (Ellefsen et al., 1991), dipole logging data may be used to estimate:

- directions of fast and slow flexural wave propagation, using wave form rotation technique (for example Alford, 1986).
- fast and slow flexural wave velocities, using wave form inversion and decomposition methods discussed in various articles (for example Thomsen, 1988 or Cheng and Cheng, 1995).

SSS

In this article we assume that the formations are of hexagonal symmetry and therefore the split waves are polarized orthogonally (as, for example, occurs when shear wave anisotropy is caused only by the fractures). In a more general case however, when thin layers and fractures are present simultaneously, it is possible that fast and slow waves will travel at a relative angle that is different than 90 degrees (Nolte and Cheng, 1995).

In the case of orthogonal propagation, four component waveform data matrix **V**(t) can be diagonalized as follows (Alford, 1986) :

$$\boldsymbol{D}(t) = \boldsymbol{R}^{-1}(\theta)\boldsymbol{V}(t)\boldsymbol{R}(\theta) \qquad (1)$$

Where θ is the angle between the direction of the fast shear wave propagation and the dipole X source plane of excitation.

Also:

$$\boldsymbol{V}(t) = \begin{bmatrix} Vxx(t) & Vyx(t) \\ Vxy(t) & Vyy(t) \end{bmatrix} \quad (2)$$

and the rotation matrix **R** that has diagonal form as:

$$\boldsymbol{R}(\theta) = \begin{bmatrix} Cos(\theta) & Sin(\theta) \\ -Sin(\theta) & Cos(\theta) \end{bmatrix} \quad (3)$$

$$\boldsymbol{R}^{-1}(\theta) = \begin{bmatrix} Cos(\theta) & -Sin(\theta) \\ Sin(\theta) & Cos(\theta) \end{bmatrix} \quad (4)$$

Formula (1) after evaluation will yield four components:

$$\boldsymbol{R}xx(t,\theta) = Cos(\theta)Vxx(t)Cos(\theta) - Cos(\theta)Vxy(t)Sin(\theta)) - Sin(\theta)Vyx(t)Cos(\theta) + Sin(\theta)Vyy(t)Sin(\theta) \quad (5)$$

$$\boldsymbol{R}xy(t,\theta) = Sin(\theta)Vxx(t)Cos(\theta) + Cos(\theta)Vxy(t)Cos(\theta)) - Sin(\theta)Vyx(t)Sin(\theta) - Cos(\theta)Vyy(t)Sin(\theta) \quad (6)$$

$$\boldsymbol{R}yx(t,\theta) = Sin(\theta)Vxx(t)Cos(\theta) - Sin(\theta)Vxy(t)Sin(\theta)) + Cos(\theta)Vyx(t)Cos(\theta) - Cos(\theta)Vyy(t)Sin(\theta) \quad (7)$$

$$\boldsymbol{R}yy(t,\theta) = Sin(\theta)Vxx(t)Sin(\theta) + Sin(\theta)Vxy(t)Cos(\theta)) + Cos(\theta)Vyx(t)Sin(\theta) + Cos(\theta)Vyy(t)Cos(\theta) \quad (8)$$

All four components shown above represent the usual Alford rotation equations. Typically, in order to get fast shear direction, off axis components ($\boldsymbol{R}xy$ or $\boldsymbol{R}yx$) are minimized (with respect to θ) - most frequently the least-squares method is used. If wave form data is of good quality, the least-squares technique will deliver robust results. However, when the signal to noise ratio is poor, or if mixed acoustic modes are present within recording window, then the least-squares method will encounter convergence problems. Simply stated - the regression and least-squares techniques might not be adequate.

PROCESSING METHOD

Time domain guided shear wave anisotropy analysis is described below as a series of separate processing steps. Each step is explained and results are presented and discussed.

#1. Transmitter Data Collocation. This step is required only if the X and Y dipole transmitters are not physically co-located. If the logging step is equal to the receiver interspacing, then some of the waveforms will have to be reduced. For example, assuming that transmitters X and Y are mis-collocated by 12 inches, and that receiver interspacing is equal to 6 inches, then two receiver wave forms created by each of dipole excitations will have to be discarded. This process, although quite simple conceptually, might introduce errors due to tool spinning between two consecutive shots. In other words, after "enforced" collocation, transmitters X and Y azimuthal positions might not be orthogonal.

#2. Flexural Wave Time Domain Tracking. Flexural wave arrival time is tracked at each receiver station independently. The travel time searching routine is repeated twice: first utilizing dipole XX (on axis) data, and then dipole YY (also on axis) data. During each of the passes, the faster arrival is selected, thus yielding the vector of depth domain curves that define zero phase arrival time independently at each receiver level. Under isotropic conditions, since the transmitter data are collocated, dipole XX and dipole YY zero phase arrival times will be the same. However, when the formation is anisotropic, they will differ by the strength of the anisotropy field. This procedure is essential. It assures that the fast flexural wave will always be located within processing window position in time domain. **Figures 1** and **2** show an example of dipole XX and YY flexural wave forms, together with imposed arrival times obtained in slow formation. A strong compressional wave is evident in the front of flexural arrivals. Flexural data is generally of good quality – there are only a few narrow depth intervals where the signal to noise ratio drops to lower values. **Figure 3** presents flexural wave travel time tracking results obtained with dipole XX (brown), and dipole YY (blue). At the top of the log, dipole XX travel time is substantially faster than the one obtained with dipole YY. A reversed effect is observed over the bottom depth zone, thus indicating that shear wave azimuthal anisotropy might be present. This is confirmed in **Figure 4,** illustrating minimum of XX vs. YY travel times (brown), and tool azimuth log (black). Tool angular position shows rapid spin from approximately 90 degrees at the top zone, down to an average of 20 degrees at the bottom part of the log. **Figures 5** and **6** show the first receiver XX and YY waveforms with imposed minimum travel time curve.

SSS

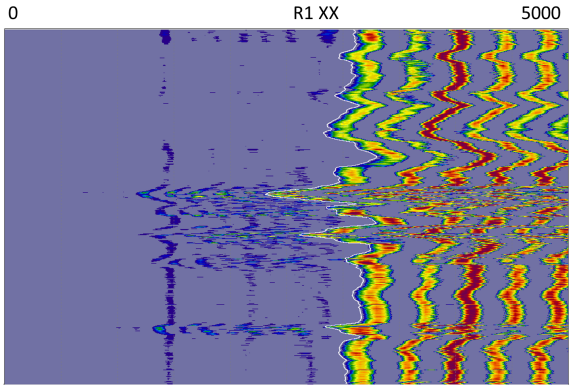

Figure 1. Near receiver dipole XX wave forms shown with imposed arrival time.

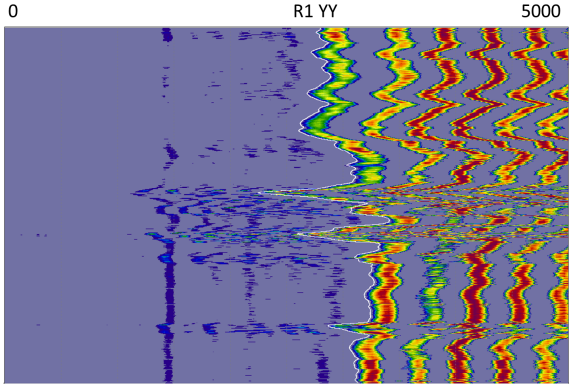

Figure 2. Near receiver dipole YY wave forms shown with imposed arrival time.

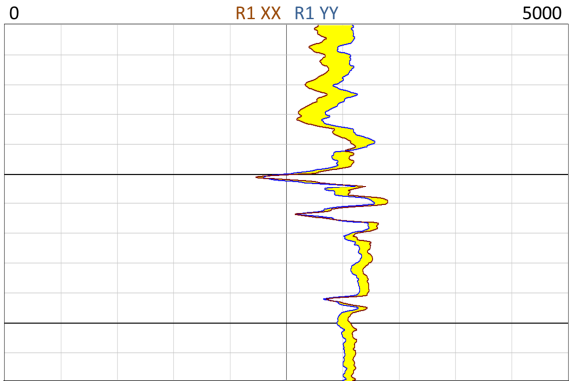

Figure 3. Flexural wave travel time tracking results obtained with dipole XX (brown), and dipole YY (blue). At the top of the log dipole XX travel time is substantially faster than the one obtained with dipole YY. Reversed effect is observed over the bottom depth zone.

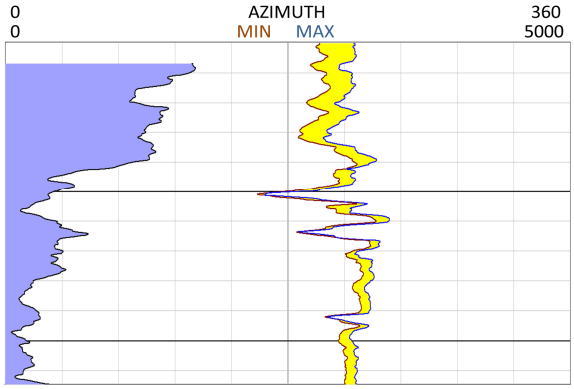

Figure 4. Minimum (brown) and maximum (blue) of XX and YY travel time curves obtained from the logs presented in Figure 3. Tool azimuth (black) shows rapid spin from ~90 degrees at the top zone, down to ~20 degrees at the bottom part of the log.

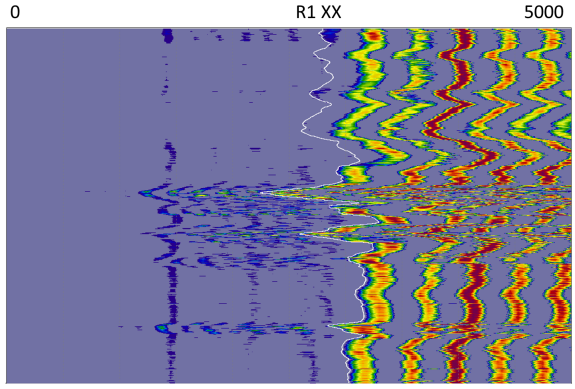

Figure 5. The first receiver dipole XX wave forms with imposed minimum arrival time.

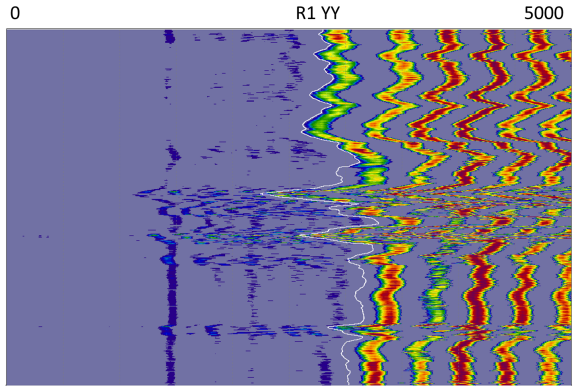

Figure 6. The first receiver dipole YY wave forms with imposed minimum arrival time.

SSS

#3. Angular Energy Distribution. Using time domain tracking profiles (computed in step **#2**), and wave form rotation formulas (5, 6, 7, and 8), angular energy distributions are calculated as follows:

$$\boldsymbol{E}(\theta) = \sum_{t=tstart}^{t=tstop} [\boldsymbol{R}^{-1}(\theta)\boldsymbol{V}(t)\boldsymbol{R}(\theta)]^{\mathbf{2}} \qquad (9)$$

Where $\boldsymbol{E}(\theta)$ is four component angular energy matrix.

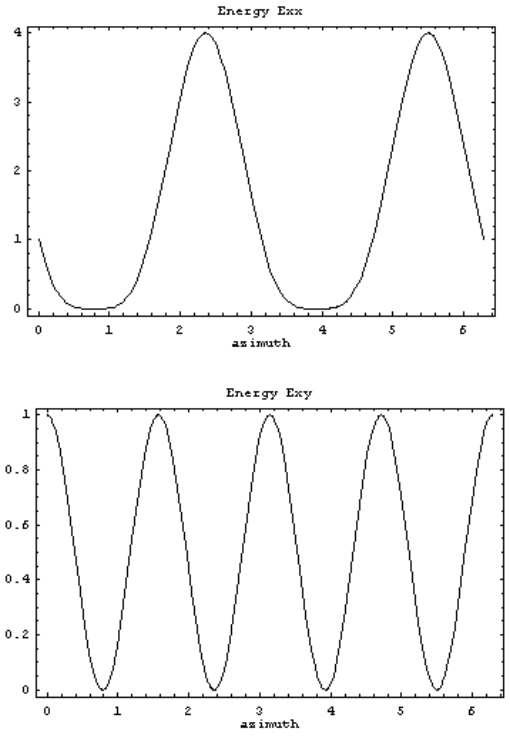

Figure 7. Angular energy matrix components E_{xx} and E_{xy} obtained under perfect anisotropic conditions (e.g $Vxx = Vyy,\ Vxy = Vyx$), computed from equation (9).

Thus if the formation is anisotropic, the on axis angular energy distributions will contain two clearly defined maxima and minima, separated by 180 degrees. The off axis angular energy distributions will contain four local maxima and minima, separated by 90 degrees. Local maxima of the on axis energy component are in phase with the local minima of off axis component. Also, on axis and off axis E_{yy} and E_{yx} components will be shifted by 90 degrees with respect to E_{xx} and E_{xy} respectively.

Since the signals are discrete the *tstart* and *tstop* limits in equation (9) represent the first and last time domain samples of the desired range of summation. Four energy components are computed at each receiver level separately for on axis E_{xx}, $E_{yy,}$ and off axis E_{xy}, E_{yx} fields. A unique feature of this algorithm is that the energy distribution computations are guided (i.e. start time is varying as a function of depth) and performed within a relatively narrow time band; thus reducing the possibility that non-flexural mode waveforms (e.g. Stoneley or compressional mode) can contaminate the outcome. The width of the time window is usually fixed and covers one to three wave cycles;depending on the formation properties. Also, since the rotation matrix components are periodic, the azimuth angle θ varies from 0 up to 2π only. **Figures 8** and **9** present on axis E_{xx} and off axis E_{xy} energy distributions (receiver #1 and #8 for image clarity) obtained over anisotropic interval. Note that the angular position of the maximum of on axis energy E_{xx} fits very well into the minimum of off axis energy E_{xy} as was predicted from formula (9). Finally, on axis E_{yy} and off axis E_{xy} components are the same as E_{xx} and E_{xy} respectively - the only difference being a 90 degree shift between them (compare **Figures 8**, **9**, **10**, and **11**).

The observations above yield the following conclusion: in order to get azimuthal maximum stress direction, either the minimum of off axis energy E_{xy}, or the maximum of on axis energy E_{xx} can be tracked. In other words, if off axis energies are noisy then on axis energies can be used, and vice versa. Dipole Y energy components might also be used.

SSS

The results of anisotropy analysis obtained with data recorded under difficult borehole conditions (washed out zone up to 14 inches in diameter) are shown on the **Figures 12** (predicted from formula (9)) and **Figures 13**, **14**, **15**, and **16** (well data). The pattern of 2 on axis E_{xx} energy picks accompanied by 4 off axis E_{xy} energy picks is getting less visible. Also, the ratio between the maximum and minimum of on axis energies is getting lower, especially over bottom part of the interval.

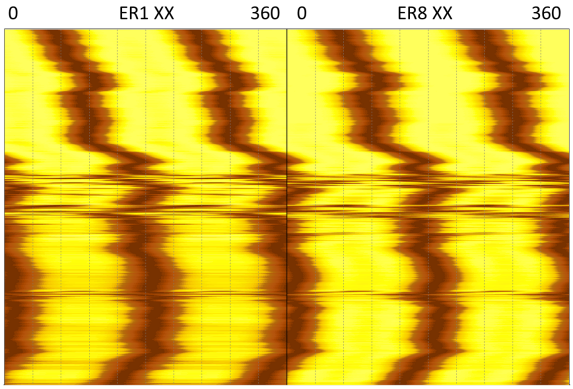

Figure 8. Near and far receiver E_{xx} angular energy distributions, obtained over anisotropic intervals.

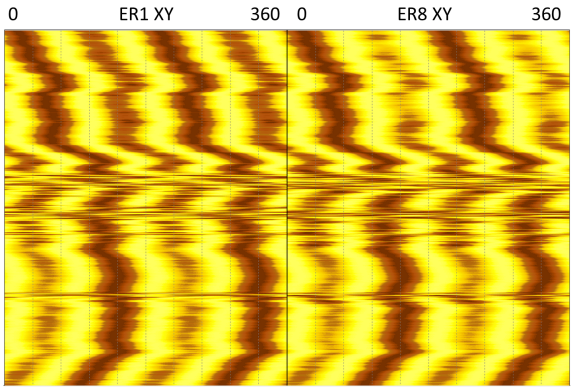

Figure 9. Near and far receiver E_{xy} angular energy distributions, obtained over anisotropic intervals.

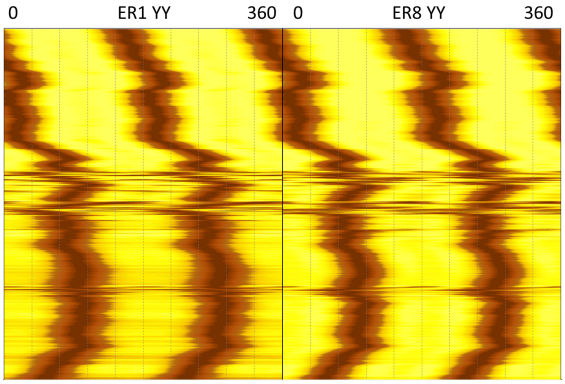

Figure 10. Near and far receiver E_{yy} angular energy distributions, obtained over anisotropic intervals.

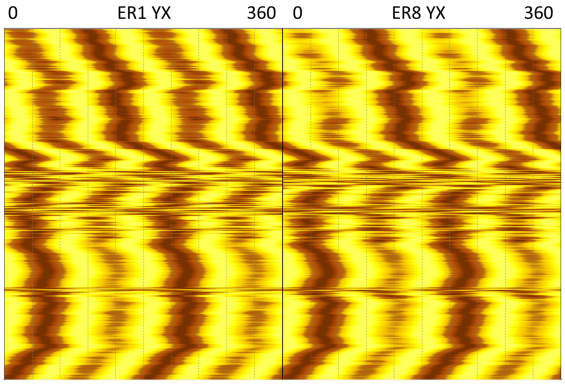

Figure 11. Near and far receiver E_{yx} angular energy distributions, obtained over anisotropic intervals.

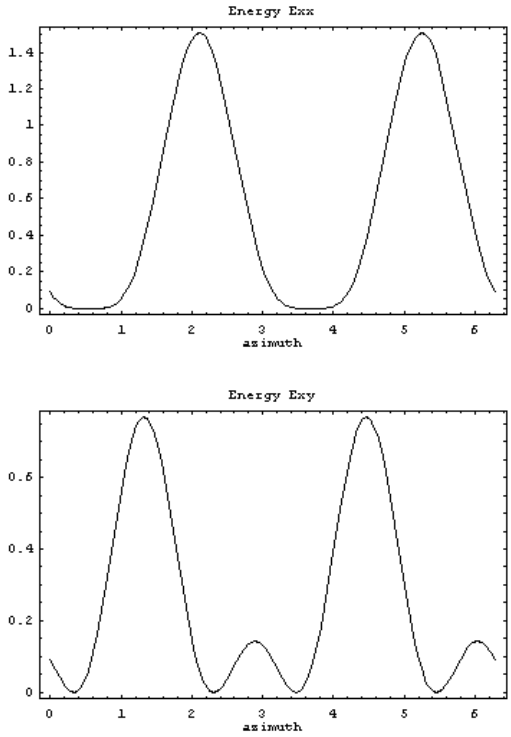

Figure 12. Angular energy matrix components E_{xx} and $E_{xy,}$ obtained under difficult borehole conditions (e.g $Vxx \neq Vyy$, $Vxy \neq Vyx$), computed from equation (9).

SSS

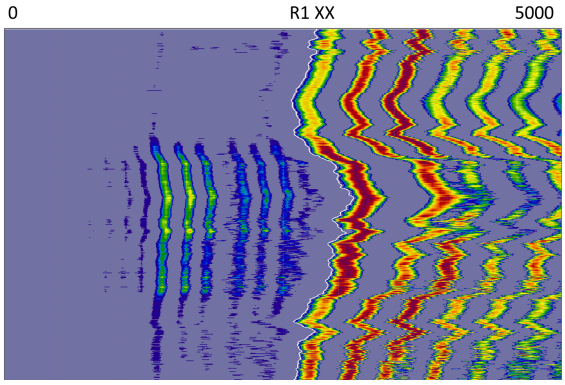

Figure 13. Near receiver dipole XX wave forms recorded over washed out zone, with imposed flexural wave arrival time.

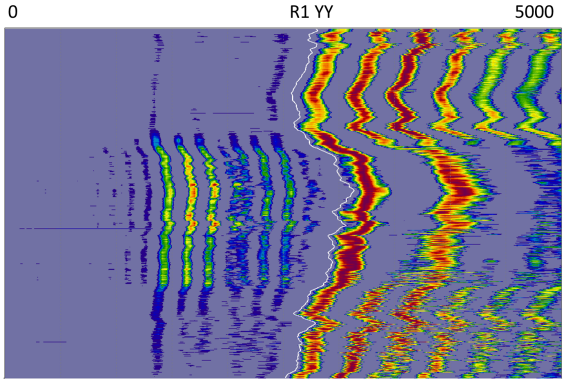

Figure 14. Near receiver dipole YY wave forms recorded over washed out zone, with imposed flexural wave arrival time.

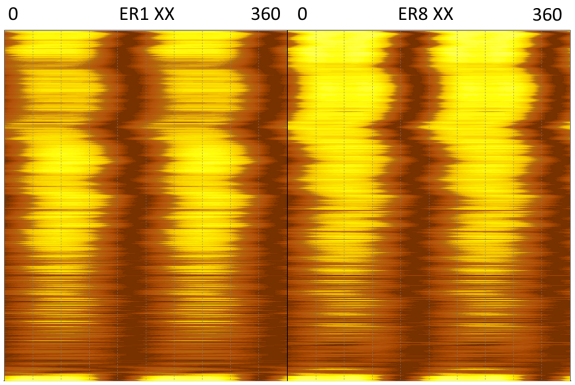

Figure 15. Near and far receiver E_{xx} angular energy distributions, obtained over washed out zone.

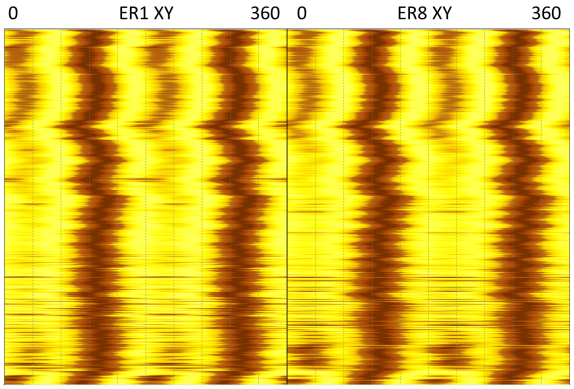

Figure 16. Near and far receiver E_{xy} angular energy distributions, obtained over washed out zone.

The conclusion is that even under washed out conditions a pattern of 0 degrees shift between the maximum of on axis energy E_{xx} and the minimum of off axis energy E_{xy} is still indicated, although this effect is much less obvious. Also, the pattern of 2 on axis energy peaks by 4 off axis energy peaks vanishes, especially over washed out interval. This effect can be used to identify Stoneley mode contamination (due to the possibility of tool decentralization due to the wash out).

Figures 17 and **18** below show results obtained while guiding anisotropy analysis using various arrival profiles. In each case, the time window position was shifted evenly by 250 uSec towards the end of the wave train. A constant window width of 500 uSec was applied. The depth domain arrival profile was the same for each test.. It is clearly noticeable that the pattern of 2 by 4 maxima and minima gradually shifts to a 4 by 4 pattern as one samples later into the wave train. This effect is also confirmed by theoretical predictions shown on **Figure 19**, and can be used to identify erroneous window position in time domain.

Figures 20 and **21** present results obtained when a proper time window position is selected but its width is too broad (1500 uSec in this case). The conclusion here is that as long as the time window position is correct, a time band that is too broad will contaminate angular energy components, making it significantly more difficult (although still possible) to track the peaks of the energies.

SSS

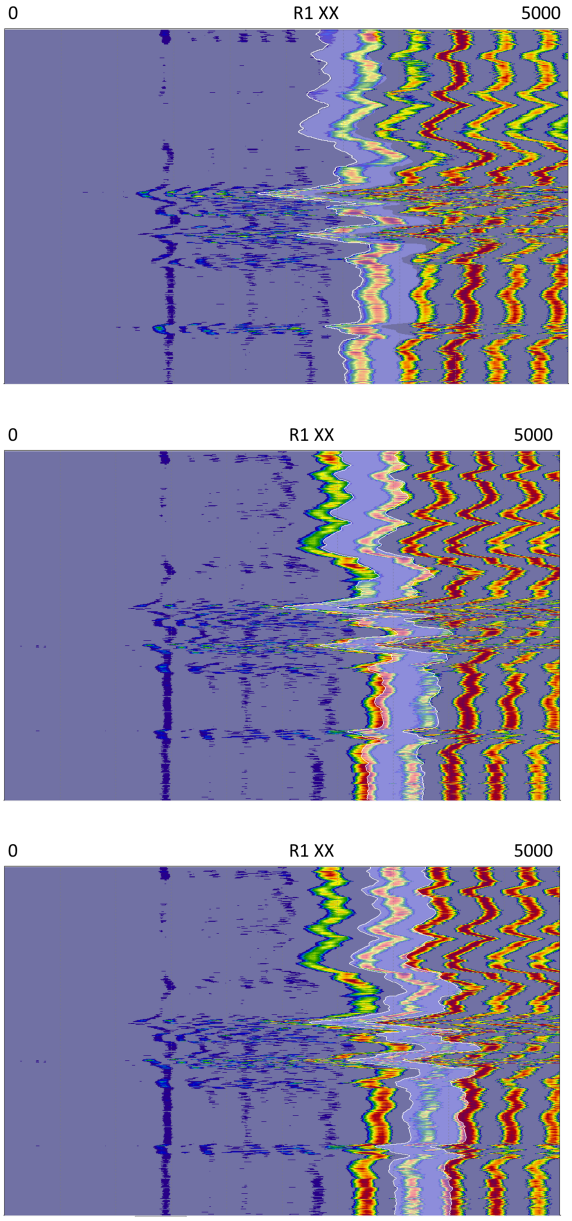

Figure 17. Near receiver dipole XX wave forms with imposed processing time window. For each case time window position was shifted by 250 uSec toward the end of recorded wave train.

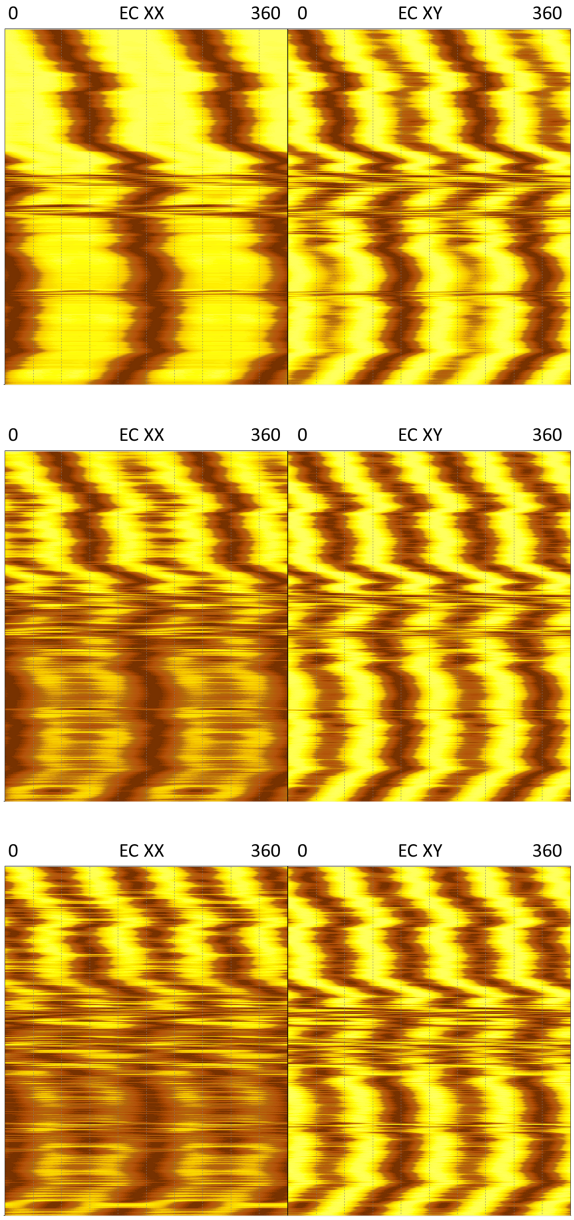

Figure 18. Near receiver dipole X (on axis E_{xx} - left track), and dipole XY (off axis E_{xy} - right track), angular energy distributions obtained over anisotropic intervals. Corresponding processing time window position and its width are shown on **Figure 17**.

SSS

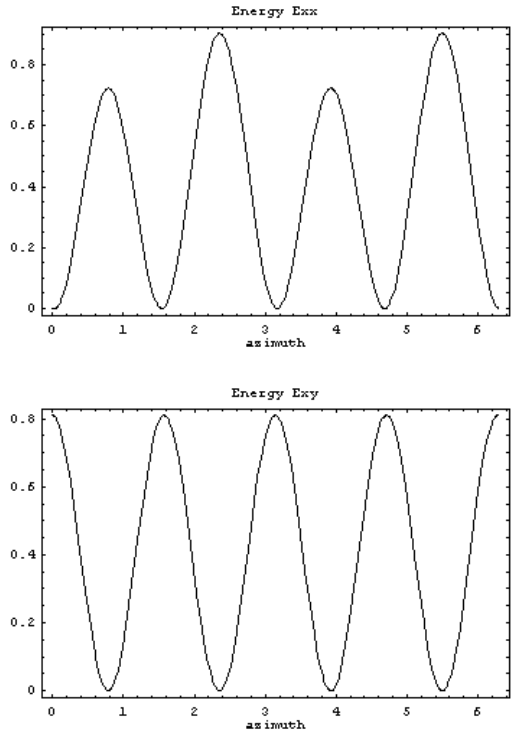

Figure 19. Angular energy matrix components E_{xx} and $E_{xy,}$ obtained with time window position allocated too deeply into the wave train, computed from equation (9).

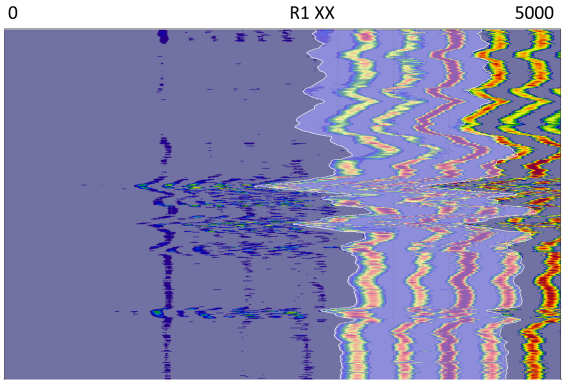

Figure 20. Near receiver dipole XX wave forms with imposed processing time window, and its width (broad band).

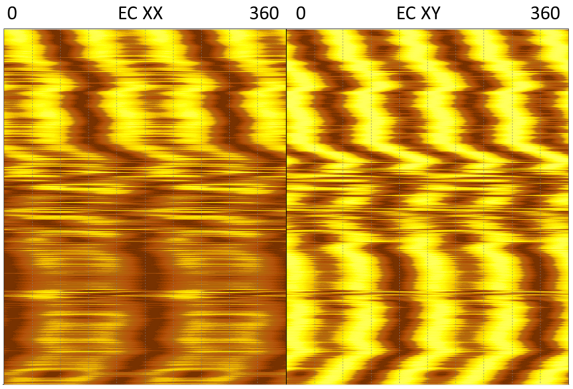

Figure 21. Near receiver dipole XX (on axis left track) and dipole XY (off axis - right track) angular energy distributions obtained over anisotropic intervals. Corresponding processing time window position and its width are shown on **Figure 20**.

#4. Angular Energy Distribution Stack. In order to improve the signal to noise ratio, the angular energy distribution data computed in previous steps are stacked together across the receiver array. This operation does not significantly degrade vertical resolution because shear wave anisotropy, if present, manifests itself along considerable depth intervals rather than within thin bed boundaries.

SSS

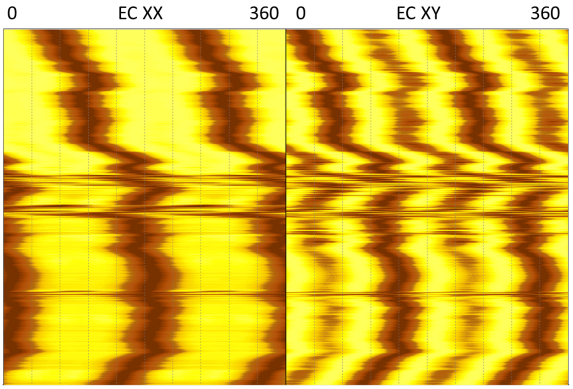

Figure 22. Near receiver dipole XX (on axis left track), and dipole XY (off axis right track) angular energy distributions, obtained after stacking individual responses across the receiver array.

#5. Wave Form Rotation Angle. If the formation is anisotropic, the on axis angular energy distribution will contain two clearly defined maxima and minima separated by 180 degrees. The off axis angular energy distribution will contain four local maxima and minima

separated by 90 degrees (see theoretical predictions presented in **Figure 7**). The waveform rotation angle is tracked through one of the troughs of off axis energy E_{xy} component that is in phase with an E_{xx} energy peak. A key quality control indicator will be how well the waveform rotation angle correlates with the magnetically derived logging tool azimuth curve. If the formation is isotropic, on/off axis energies either don't show peaks, or their appearance will be fuzzy and the resulting waveform rotation angle curve will not correlate well with the tool azimuth data.

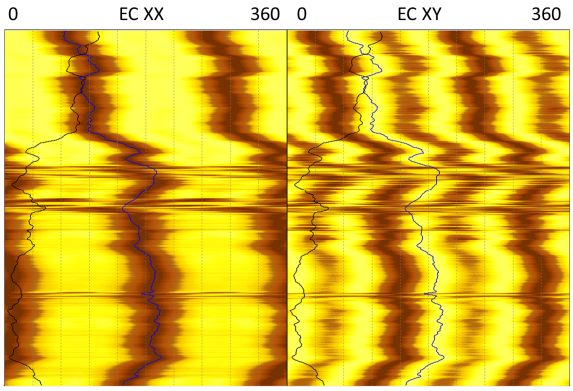

Figure 23. Dipole X angular energy distributions E_{xx} and $E_{xy,}$ shown with imposed tool azimuth (pad - black curve), and the minimum of off axis energy (blue).

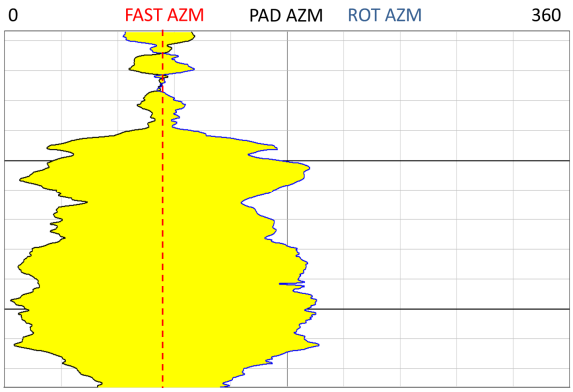

Figure 24. Magnetically derived tool azimuth (pad - black curve) and minimum of off axis energy E_{xy} (blue curve) are presented. Note excellent agreement between directional package and dipole tool derived rotation azimuth. Fast shear azimuth can be computed from modulo 360 degrees arithmetic on the tool azimuth and rotation curves.

#6. Rotation, Fast and Slow flexural DTS. Using the waveform rotation angle, original data (all cross dipole components), and the rotation formulas, the fast and slow flexural mode waveforms are generated. Depending on the signal to noise ratio of the rotated flexural modes, IFS (Instantaneous Frequency Slowness) Analysis or phase method (Kozak, Boonen, and Seifert, 2001), Guided Semblance Analysis, or a combination of both methods may be used to compute fast and slow flexural wave slowness logs. Fast shear wave azimuth can also be calculated.

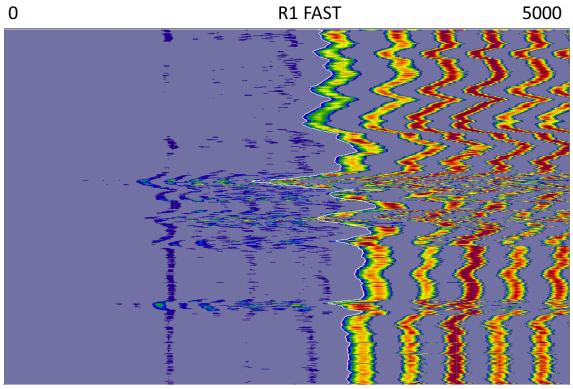

Figure 25. Near receiver post rotated fast flexural wave forms, shown together with fast wave arrival time.

SSS

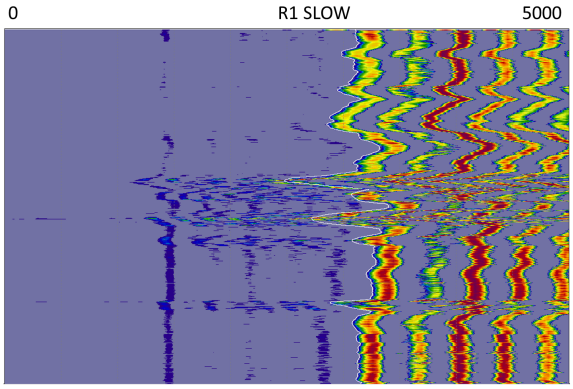

Figure 26. Near receiver post rotated slow flexural wave forms, shown together with slow wave arrival time.

Whether semblance and IFS methods areused to compute fast and slow flexural slowness curves, waveforms should be guided in time domain. Applying a relatively narrow time window width in the picking process assures that potentially competing acoustic modes arrive outside of the processing window.

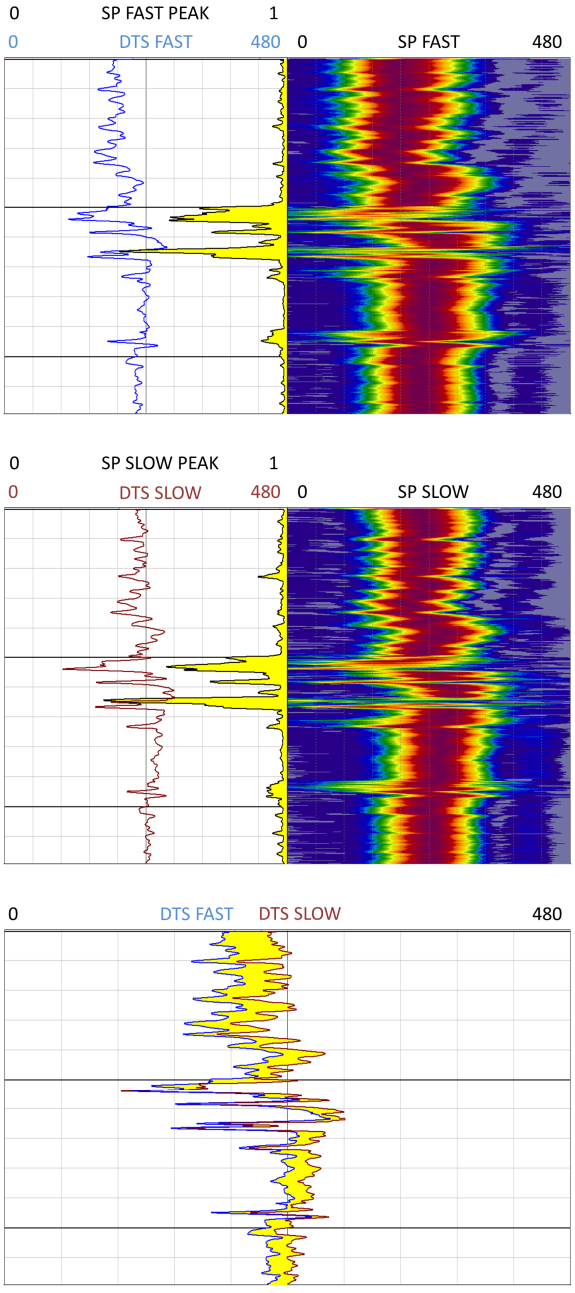

Figure 27. Results of fast and slow flexural waves processing, obtained with semblance method. Tracks #1 show DTS fast (blue), DTS slow (brown) and semblance projection peak value logs. Tracks #2 present fast and slow semblance projection wave forms. Bottom picture shows magnified comparison between fast and slow flexural wave slowness curves.

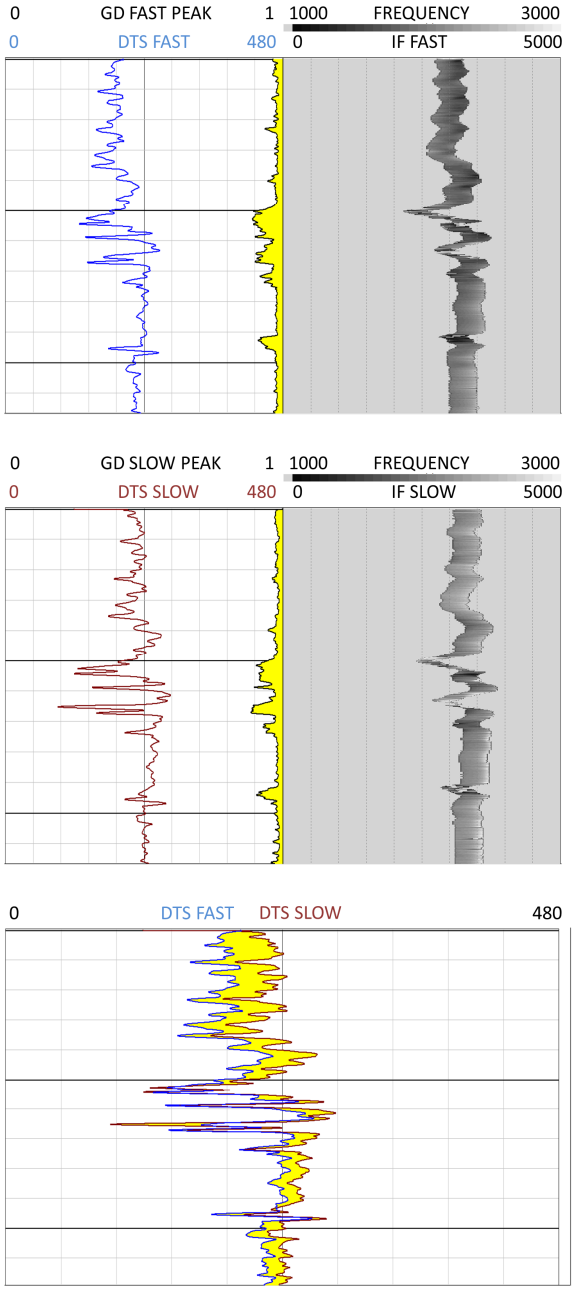

Figure 28. Results of fast and slow flexural waves processing, obtained with instantaneous frequency-slowness method. Tracks #1 show DTS fast (blue), DTS slow (brown) and goodness peak value logs. Track #2 present fast and slow instantaneous frequency waveforms. Bottom picture shows comparison between fast and slow flexural wave slowness curves.

SSS

#7. Quality Control Measures. Angular energy distribution wave forms are computed at each receiver level separately (e.g. on axis E_{xx} and $E_{yy,}$ and off axis E_{xy} and E_{yx} fields). Each energy component consists of an array of 8 vectors derived from dipole X and Y excitations. Standard deviation and coherence computations are performed (in azimuth domain). Since angular response at each receiver station should be similar, then under good well conditions standard deviation of each energy component ought to be close to 0 degrees. Also, the coherence should be close to 1 – characteristic similar to semblance projection peak value.

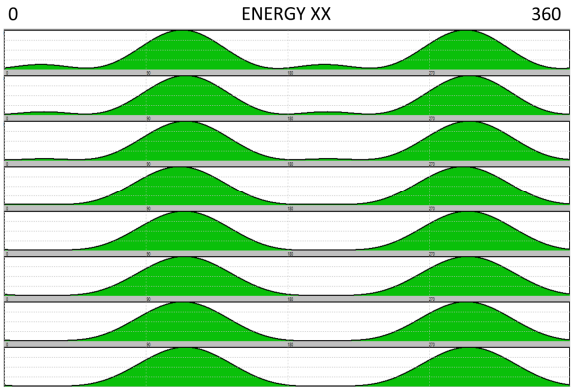

Figure 29. Example of E_{xx} azimuthal signature of dipole X energy obtained over anisotropic intervals.

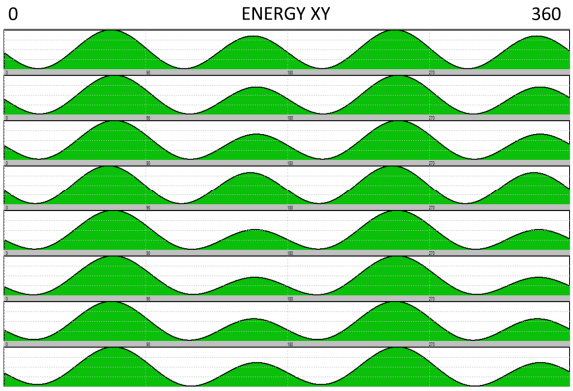

Figure 30. Example of E_{xy} azimuthal signature of dipole X energy obtained over anisotropic intervals.

Finally, cross dipole elements created during the waveform rotation can be used to get post rotated energy distribution components. If the anisotropy analysis was performed correctly, the resulting energy E_{xx} should peak at 0 or 180 degrees relative to the tool; meaning no further rotation is needed. Also the 2 by 4 peaks pattern ought to be present. Furthermore, all four energy components E_{xx}, E_{xy}, E_{yx}, and E_{yy} should havea flat depth invariant appearance (see **Figure 32** below).

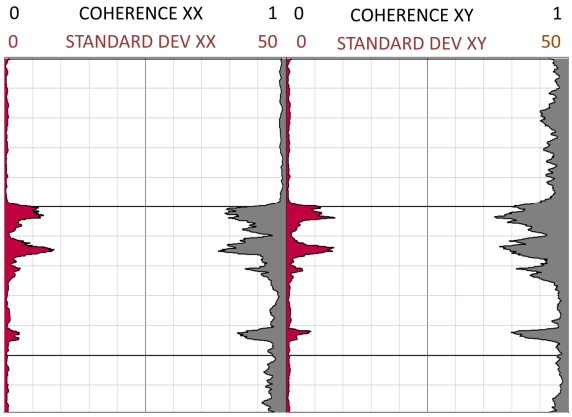

Figure 31. Track #1 shows coherence (black) and standard deviation (brown) curves of on axis E_{xx} energies. Track #2 shows coherence (black) and standard deviation (brown) of off axis E_{xy} energies. Long term average standard deviation approaches 2 degrees while the coherence is at the level of 0.85 or higher.

SSS

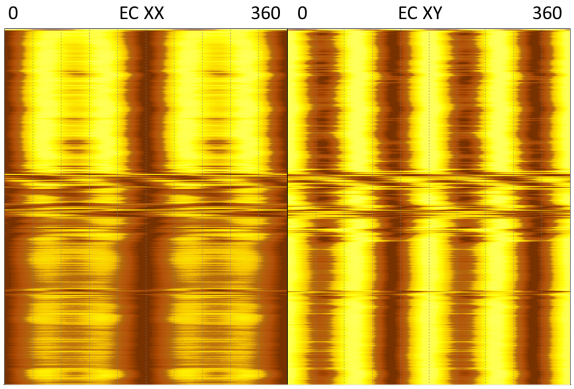

Figure 32. Near receiver dipole XX (on axis E_{xx} - left track) and dipole XY (off axis E_{xy} - right track) angular energy distributions obtained after waveform rotation.

CONCLUSIONS

A modified technique for processing cross dipole acoustic data that is based on guiding in time domain has been presented and discussed. This method works very well in vertical to moderately inclined wells. This technique is weakly sensitive to the position and width

of the processing window in time domain. The method produces information that may be used to identify mixed acoustic mode contamination present within the processing window -for example due to Stoneley mode. The technique also generates various quality measures, including coherence and standard deviation of energy components across receiver array. Theoretical predictions were compared against real data.

REFERENCES

Alford, R.M., 1986. Shear data in presence of azimuthal anisotropy, 56th Annual International

Ellefsen, K. J., Cheng, C.H., and Toksoz, M.N., 1991, Effects of anisotropy upon the normal modes in a borehole, J. Acoustic Society, Am., 89, 2597-2616

Kozak, M., Boonen, P., Seifert D., 2001, Phase velocity processing for acoustic logging-while-drilling full wave form data, SPWLA proceedings.

Kurkjian, A.L., Chang, S.K., 1986, Acoustic multipole sources in fluid-filled boreholes, Geophysics, v. 51, p. 148-163.

Nolte, B., Cheng, C.H., 1995. Observation of flexural wave anisotropy from cross-dipole logs in the Powder River Basin, Wyoming, Earth Resources Laboratory, MIT.

Tanner, M. T., Koehler, F., Sheriff, R.E., 1979, Complex trace analysis, Geophysics, v. 44, p. 1041-1063.

Thomsen, L., 1988. Reflection seismology over azimuthally anisotropic media, Geophysics, 53, 304-313.

ABOUT THE AUTHORS

Marek Kozak is a cofounder of Supersonic Geophysical LLC located in Newark, California. He holds a Ph.D. in EE/ Measurement Systems from the Warsaw University of Technology in Poland. He has been instrumental in the development of pulsed power wire line induction and acoustic logging tools, and data processing software. Prior to arriving to USA in 1990 he was with the Warsaw University of Technology, conducting research in theoretical and applied magnetics sponsored by Polish Academy of Sciences, teaching classes in measurement of non-electrical quantities, and working as the industry consultant in DSP systems. He is a member of IEEE, SEG and Planetary Society.

Mirka Kozak holds Master's Degrees in Computer Science and Electrical Engineering from the Warsaw University of Technology in Poland. Prior to arriving to USA she was working at the Institute of Computer Science in Warsaw, Poland, as a researcher in the wide area networking systems. In 1992 she joined Magnetic Pulse Inc. and in 2004 Supersonic Geophysical LLC, as a Software Development Engineer instrumental in the development of induction and acoustic data processing software. She is a member of IEEE.

Jefferson Williams is a co-founder of Supersonic Geophysical LLC. He possesses Bachelor's degrees in Geology and Mechanical Engineering as well as Master's Degrees in Electrical and Civil Engineering. He started his career as a seismologist for Geophysical Services Inc. and later became a Field Engineer for Gearhart Industries. Later, he joined MPI where he was a Field and Maintenance Engineer as well as a Log Analyst specializing in acoustic logs. After consulting in borehole acoustics for a number of years, he co-founded Supersonic Geophysical in 2001. He is a member of SEG and SPWLA.

SSS

SSS